Diols Production From Glycerol Over Pt-Based Catalysts: On the Role Played by the Acid Sites of the Support

Diols production from glycerol over Pt-based catalysts: on the role played by the acid sites of the support

Alberto Villa,[1] Maela Manzoli,[2] Floriana Vindigni,[3] Lidia E. Chinchilla,[4] Gianluigi A. Botton,[4] and Laura Prati [1,*]

[1] *Dipartimento di Chimica, Università degli Studi di Milano, via Golgi 19, I-20133Milano, Italy*

[2] *Dipartimento di Scienza e Tecnologia del Farmaco and NIS Interdepartmental Centre, Università degli Studi di Torino, Via P. Giuria 9, 10125 Torino, Italy.*

[3] *Dipartimento di Chimica and NIS Interdepartmental Centre, Università di Torino, Via P.Giuria 7, 10125 Torino, Italy.*

[4] *Canadian Centre of Electron Microscopy and Department of Materials Science and Engineering, McMaster University 1280 Main Street West, Hamilton, Ontario L8S 4M1 (Canada)*

Corresponding author

Laura Prati

Dipartimento Chimica, via Golgi 19, I-20133Milano, Italy

e mail: Laura.Prati@unimi.it

Abstract:

A series of 1%wt. AuPt (6:4) catalysts were prepared by sol immobilization using acidic (TiO_2, H-Mordenite, SiO_2, MCM-41, Sulphated ZrO_2 (S-ZrO_2)) and one basic (MgO) oxide supports. EDX analysis showed that only alloyed AuPt nanoparticles are present on all catalysts but the final size of AuPt particles is significantly affected by the support. Indeed, on TiO_2 the mean AuPt nanoparticles diameter is 3.7 nm whereas for all the remaining support larger AuPt nanoparticles with diameter of 6-7.5 nm were obtained. AuPt catalysts result very active in catalyzing the liquid phase hydrogenolysis of glycerol to 1,2-propandiol with ethylene glycol, 1-propanol and 2-propanol as main by-products

The role of the support has been highlighted in terms of acidic properties, the medium strength of Lewis acid sites of TiO_2 leading to the best performance in terms of activity, selectivity and stability of the catalytic system.

Introduction

The use of biomass for the production of renewable raw materials and their conversion to high value chemicals and materials shows a significant potential [1-3]. The utilization of vegetable oil for the production of biodiesel has led to an increase in glycerol production, as it constitutes the main co-product (about 20% wt). Glycerol is a highly functionalized molecule, which is recognized as a promising chemical building block for the synthesis of fine chemicals [1-6]. One attractive route involves the catalytic hydrogenolysis of glycerol to diols and alcohols (as reported in Scheme 1) [7-9].

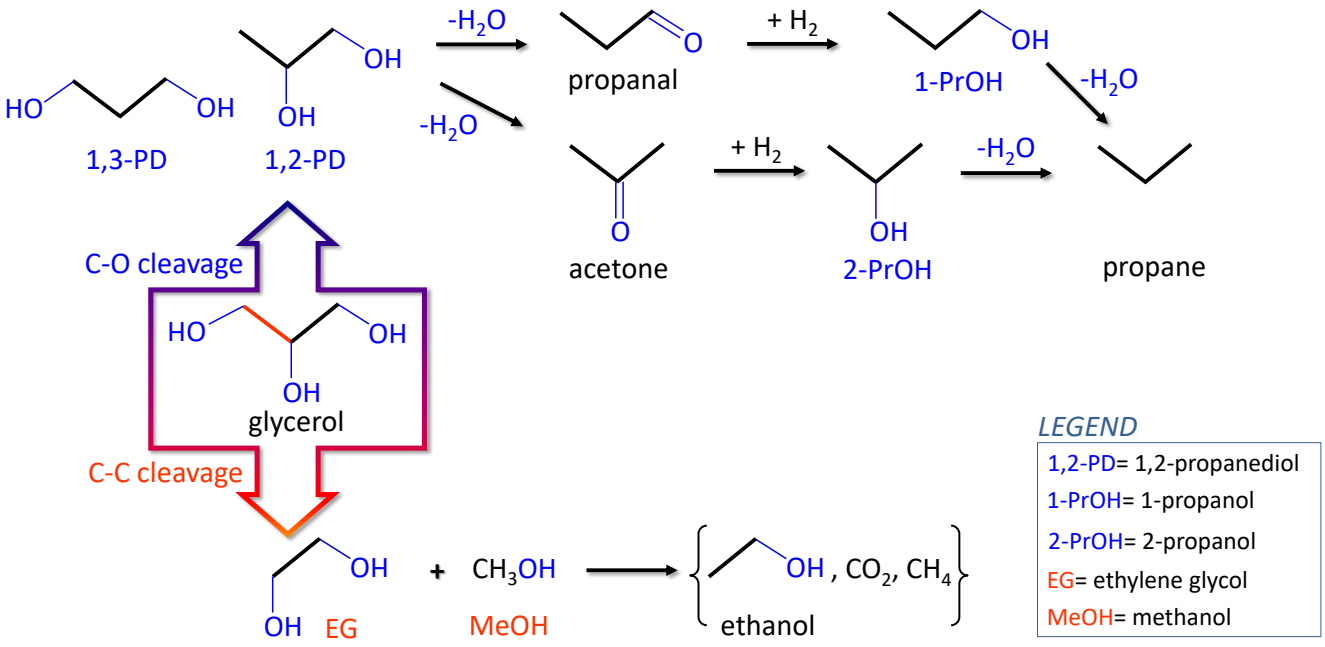

Scheme 1. Valuable chemicals obtained by glycerol .

1,2-PD, is commercially produced from propylene oxide and it is an important chemical for the production of polyesters, resins, and polyurethanes [10]. 1,3-PD is an important monomer utilized for the production of polyester fibers and films [11]. EG is produced via hydration of ethylene oxide and it is used as antifreezing agent [12].

In the past decade, glycerol hydrogenolysis has been extensively studies using different metal based catalysts, including Pt, Ru, Ni and Cu [7-9]. Among all noble metal based catalysts, Pt has been recognized as one of the most effective in the glycerol hydrogenolysis to 1,2-PD [7-9]. For example, commercial Pt/C showed high selectivity to 1,2-PD (82.7%) but only at low conversion (35%) [13]. Similar results were obtained using $PtSn/SiO_2$ with a good selectivity to 1,2-PD (84%) but even at lower conversion (16%) [14]. Nevertheless, the drawback of most of the monometallic Pt systems seems to be the low resistance to deactivation and the low capacity to maintain high selectivity at high conversion. We recently reported that the addition of Au to Ru improves the stability of the catalysts, maintaining a good selectivity also at high conversion [15]. Moreover, the beneficial effect of Au addition to Pt catalysts in terms of activity, selectivity and stability was already verified in the case of oxidation of glycerol [16,17]. Recent papers illustrated that the nature of the support can significantly affect the catalytic performance. In particular, the acid base properties have been reported to modify the activity and, primarily, the selectivity in the glycerol oxidation [7-9, 18]. Therefore, this study encompasses the investigation of the effect of the acid base properties of the support in AuPt catalyzed glycerol hydrogenolysis to 1,2 PD.

Many mechanisms corresponding to glycerol hydrogenolysis to 1,2 PD have been proposed, where the acidic/basic properties seem to have a key role in determining the final mechanism. Three main pathways (Scheme 2) are generally accepted: dehydration-hydrogenation, dehydrogenation-dehydration–hydrogenation and direct-hydrogenolysis [9].

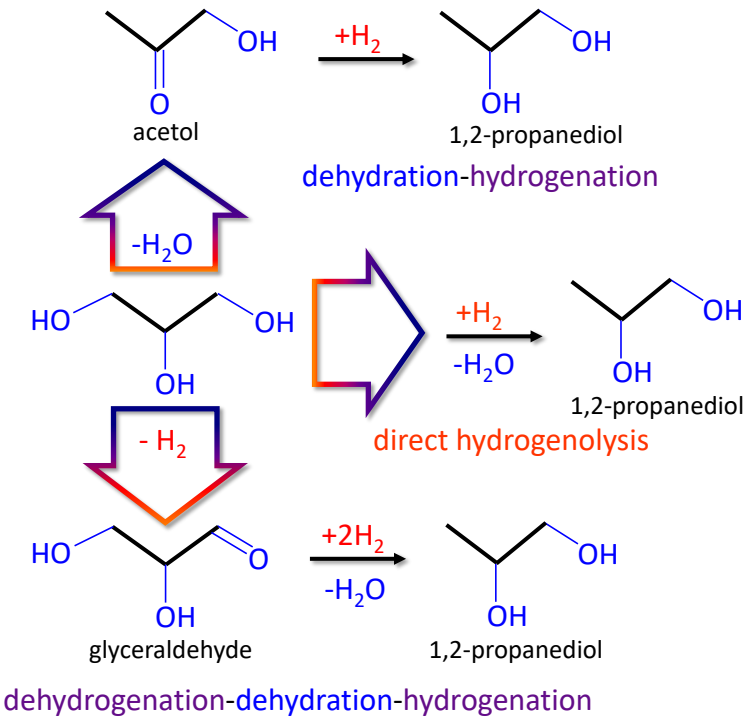

Scheme 2. Reaction pathways of glycerol hydrogenolysis.

In the first path, glycerol is initially dehydrated through an acid-catalyzed reaction to form an intermediate, which is subsequently hydrogenated to generate propanediol [19]. Following the third possible path, which usually occurs in neutral and alkaline conditions. Glycerol is dehydrogenated to glyceraldehyde with a consecutive dehydration-hydrogenation to 1,2-PD [20]. The last possibility is the direct-hydrogenolysis that was initially reported for Ir catalysts [21]: glycerol is adsorbed on the metal surface to form dihydroxyisopropoxide that is successively transformed to 1,2-PD. According to this mechanism, the low stability of the intermediate dihydroxyisopropoxide can result in the formation of over-hydrogenolysis products (1-propanol and 2-propanol). In all the possible pathways, the role of the support properties appears fundamental and yet not fully understood.

Therefore, to clarify the possible synergy between the acid base properties of the support and AuPt nanoparticles, different catalysts have been prepared supporting preformed AuPt NPs on acidic (TiO_2, H-Mordenite, SiO_2, MCM-41, S-ZrO_2) and basic (MgO) oxides. High-resolution

transmission electron microscopy (HRTEM) analysis of the AuPt catalysts was performed to investigate the morphology as well as the composition of the nanoparticles. The nature (Lewis and/or Brønsted) and acid site density were determined by a quantitative analysis of the FTIR bands of adsorbed 2,6 dimethyl-pyridine (2,6-DMP). The catalysts have been then tested in glycerol hydrogenolysis.

1. Experimental

1.1. Materials

$NaAuCl_4 \bullet 2H_2O$, and K_2PtCl_4 were from Aldrich (99.99% purity), TiO_2 P25 (SA = 48 m^2/g) was from Evonik and H-Mordenite (SA = 450 m^2/g) was from Degussa. Sulphated zirconia(SA = 78 m^2/g) , SiO_2 (SA = 148 m^2/g) and MgO (SA = 38 m^2/g) were from Alfa Aesar. MCM-41 (SA = 980 m^2/g) have been prepared following the procedure reported in ref. 22. $NaBH_4$ of purity > 96% from Fluka, polyvinylalcohol (PVA) (Mw = 13,000–23,000 87–89% hydrolyzed,) from Aldrich were used. A 1%wt PVA solution in water was prepared. Gaseous oxygen from SIAD was 99.99% pure.

1.2. Catalyst preparation

Monometallic Pt catalyst

Solid K_2PtCl_4 (0.051 mmol) and PVA (1%wt) solution (Pt/PVA 1/0.5 wt%) were added to 100 mL of H_2O. After 5 min, H_2 was bubbled (50 mL/min) under atmospheric pressure and room temperature for 2 h. The colloid was immobilized by adding the support under vigorous stirring. The amount of support was calculated as having a total final metal loading of 1 wt. %. After 2 h the

slurry was filtered, the catalyst washed thoroughly with distilled water (neutral mother liquors) and dried at 80 °C for 4 h.

Au-Pt Bimetallic catalysts

For the sake of clarity, the main steps of the preparation of the bimetallic catalysts are summarized in Scheme 3. The bimetallic AuPt catalysts were prepared by sol immobilization through a two steps procedure, which ensures the formation of alloyed bimetallic particle [16, 17].

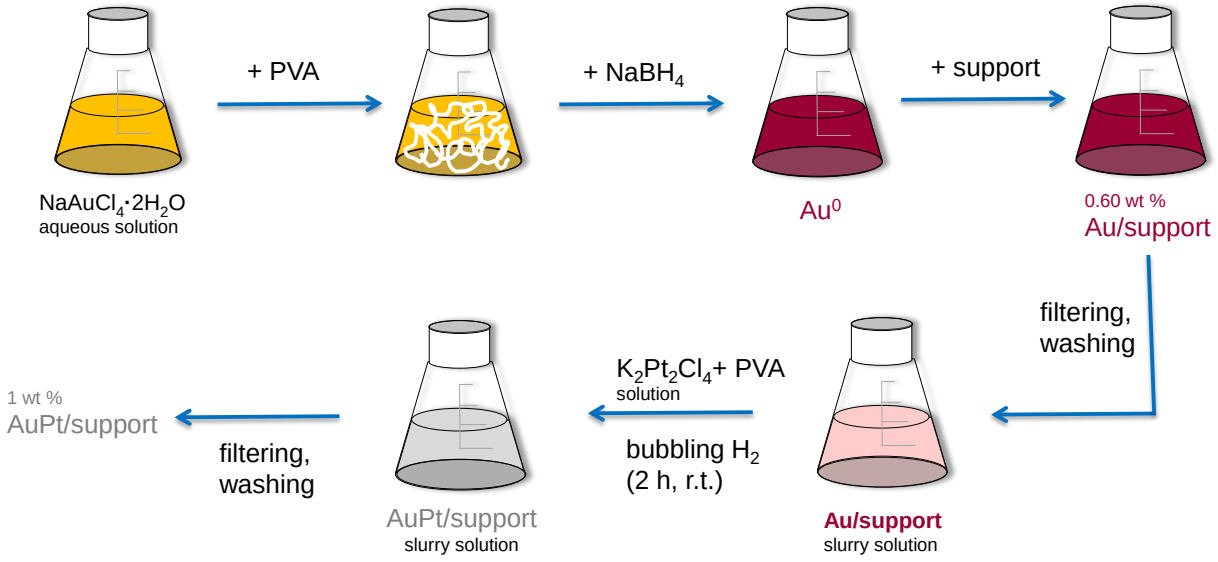

Scheme 3. Synthesis of the bimetallic catalysts.

In detail, $NaAuCl_4 \cdot 2H_2O$ (Au: 0.031 mmol) was dissolved in 60 mL of H_2O, and PVA (1%, wt%) was added (Au/PVA= 1:0.5 wt/wt). The yellow solution was stirred for 3 min, after which 0.1 M $NaBH_4$ (Au/$NaBH_4$= 1:4 mol/mol) was added under vigorous magnetic stirring. The ruby-red Au(0) sol was formed immediately. Within a few minutes of sol generation, the gold sol was immobilized by adding the support (acidified to pH 2 by sulphuric acid) under vigorous stirring. The amount of support was calculated as having a gold loading of 0.60 wt%. After 2 h, the slurry was filtered and

the catalyst washed thoroughly with distilled water (neutral mother liquors). The Au/support was dispersed in 40 mL of water, therefore K_2PtCl_4 (Pt: 0.021 mmol) and PVA solution (Pt/PVA= 1:0.5 wt/wt) were added. H_2 was bubbled (50 mL/min) under atmospheric pressure and room temperature for 2 h. After an additional 18 h, the slurry was filtered and the catalyst washed thoroughly with distilled water. ICP analyses were performed on the filtrate using a Jobin Yvon JV24 instrument to verify the metal loading on the support. The total metal loading was 1 wt%. AuPt nanoparticles were supported on five acidic oxides, i.e. TiO_2, H-Mordenite, SiO_2, MCM-41, S-ZrO_2, and a basic support (MgO). The catalysts are listed in Table 1.

1.3. Catalytic tests

Glycerol hydrogenolysis was performed at 150 °C, using a stainless steel Parr reactor (50 mL capacity), equipped with heater, mechanical stirrer, gas supply system and thermometer. The glycerol solution (30 mL; 0.3 M) was added into the reactor and the desired amount of catalyst (glycerol/ metal ratio=1000, mol/mol) was suspended in the solution. The autoclave was purged three times with nitrogen before charging 10 bar of H_2. The mixture was heated to the reaction temperature, 150°C, and mechanically stirred (1250 rpm). Products analysis: the reaction mixture, after separation from the catalysts by filtration, was analysed using high performance liquid chromatography (HPLC). Samples were removed periodically (0.5 mL) under stirring and analysed by high-performance liquid chromatography (HPLC) using a column (Alltech OA-10308, 300 mm x 7.8 mm) with UV and refractive index (RI) detection in order to analyse the product mixtures. H_3PO_4 0.1 wt% solution was used as the eluent. The identification of the possible products was done by comparison with the original samples. Activity was calculated on the total mol of metal or in alternative on the total amount of exposed surface atoms. Calculations of the number of exposed surface atoms were performed by assuming that all the nanoparticles had cub-octahedral morphology with cubic close-packed structure in this size range, the model of full-shell

nanoparticles was adopted [23]. The total number (N_t) of M atoms in the cluster for a given cluster size can be calculated using the following equation (1):

$d_{sph}= 1.105\ d_{at}N_T^{1/3}$ (1)

Where d_{sph} is the mean diameter of the Au, Pt or AuPt particles obtained from TEM analysis and d_{at} is the atom diameter of Au (0.288 nm), Pt (0.256 nm) and AuPt (0.264 nm), respectively. The number of surface atoms (N_s) and n can be calculated from equations (2) and (3), based on the values of N_T:

$N_T = (10n^3 - 15n^2 + 11n – 3)/3$ (2)

$N_s=10n^2-20n+12$ (3)

The activity based on the surface atoms can then be calculated as follows:

% of fraction of atoms lying at the surface:

$A= (N_s/N_T)\ x100$

Activity based on N_s= activity (calculated for total metal mols)/A

1.4. Characterisation

a) The metal content was checked by Atomic Absorption Spectroscopy (AAS) analysis of the filtrate, on a Perkin Elmer 3100 instrument.

b) Samples for transmission electron microscopy (TEM) characterization were prepared by depositing an ethanol suspension of the catalyst onto lacey carbon coated 300 mesh copper grids. The particle morphology of the supported nanoparticles, specifically the nanoparticle size, was first investigated by TEM using a Philips LaB_6 electron microscope, operating at 200 kV and equipped with a Gatan CCD camera. Detailed high resolution High Angle Annular Dark Field Scanning TEM (HAADF-STEM) imaging and energy-dispersive X-ray spectroscopy (XEDS) analyses were carried

out using FEI Titan3 microscope operated at 200 kV accelerating voltage for a deeper investigation of the AuPt alloy structure of AuPt/TiO_2 catalyst. This microscope is equipped with double aberration correctors, providing ultrahigh-resolution HAADF-scanning TEM (STEM) images, and an Oxford Inca energy dispersive X-ray (EDX) spectrometer equipped with a 30 mm^2 ultrathin window Si/Li X-ray detector. XEDS data were collected either as spectrum images, in which a focused electron probe was scanned across a region of interest during data collection, or in stationary spot mode, where an emitted X-ray spectrum from 0–20 kV is acquired from a specific point on a particle using a probe size less than 0.5 nm. Spectra were acquired with a probe current of approximately 0.5 nA and dwell times between 200 and 400 ms per pixel, in the case of maps, and 20-30 seconds per analysis in spot mode. STEM digital images were acquired using FEI TIA software and Oxford–INCA microanalysis software was used for XEDS acquisition and analysis. The atomic fractions of gold and platinum were quantified by the Cliff-Lorimer method on relative intensities of the Pt-Lα and Au-Lα peaks using k-factors provided by the XEDS system manufacturer. The AuPt particle size distribution and the total metal dispersion were determined by counting 250 particles in HAADF-STEM images using GAUSS software.

c) FTIR spectra were taken on a Perkin-Elmer 2000 spectrometer (equipped with a MCT detector) with the samples in self supporting pellets introduced in cells allowing thermal treatments in controlled atmospheres and spectrum scanning at room temperature (r.t.) in vacuum or in the presence of probe gases. The 2,6-dimethylpyridine (2,6-DMP) adsorption/desorption experiments were performed on the samples after activation in vacuum at 393 K for 1 hour. The following procedure was adopted: (i) inlet of an excess dose of 2,6-DMP vapor (~2 Torr), and equilibration at r.t. for 10 min; (ii) evacuation at r.t. for 30 min. From each spectrum, the spectrum of the sample before the inlet of the probe was subtracted. The spectra have been normalised with respect to the weight of the pellets and to the surface areas of the different supports.

The processing of the FTIR spectra of adsorbed 2,6-DMP was performed by using Fityk 0.9.8, an open-source curve-fitting and data analysis software, that allows to obtain the accurate curvefits

(either Gaussian or Lorentzian curves were used). As output files, the software permits the realisation of one figure each time containing the files related to one specific sample in the optimised spectral range, therefore it was not possible to plot all files in the same figure.

2. Results and Discussion

The catalysts were evaluated in glycerol hydrogenolysis (0.3 M glycerol, glycerol/metal=1000 mol/mol, 10 atm H_2, T= 150 °C) and both activity and selectivity, at isoconversion (60%) are reported for each system in Table 1.

Table 1. Catalytic evaluation in the glycerol hydrogenolysis[a]

Catalyst	Activity[b] (h^{-1}) $\frac{mol}{mol \cdot h}$	Activity A[c] $\frac{mol}{N \cdot h}$	Selectivity (%)[d]					AuPt size (nm)
			1,2-PD	1-PrOH	2-PrOH	EG	MeOH	
AuPt/MgO	34	176	93	-	-	3	2	6.9
AuPt/TiO_2	56	165	90	-	-	4	2	3.7
AuPt/MCM-41	22	111	52	-	-	22	16	6.7
AuPt/SiO_2	21	117	35	-	-	28	22	7.5
AuPt/H-Mordenite	14	65	30	8	12	20	16	6.2
AuPt/S-ZrO_2	10	52	31	10	11	18	15	6.9
Pt/TiO_2	41	119	86	-	-	3	4	3.6
Au/TiO_2	1	2	-	-	-	-	-	3.5

[a] Reaction conditions: Glycerol = 0.3M, pH_2= 7 bar, T= 150°C, metal/glycerol = 1/1000 mol/mol. EG= ethylene glycol, 1,2-PD = 1,2 propandiol, 1-PrOH = 1-propanol
[b] Mol of glycerol converted per hour per mol of metal, calculated after 0.5 hour of reaction
[c] Mol of glycerol converted per hour per fraction of atoms lying at the surface, A (A=(Ns/NT) x100) after 0.5 hour of reaction.
[d] Selectivity at 60% of conversion

The activity was calculated firstly basing on the moles of glycerol converted per hour per total mol of metal. By using this approach, AuPt/TiO_2 showed a high activity (56 converted mol of glycerol (AuPt mol)$^{-1}$ h^{-1}), superior than AuPt supported on MgO (34 converted mol of glycerol (AuPt mol)$^{-1}$ h^{-1}) and the other acidic oxides (<22 mol of glycerol (AuPt mol)$^{-1}$ h^{-1} for AuPt/MCM41, AuPt/SiO_2, AuPt/H-Mordenite, AuPt/S-ZrO_2, accordingly). Moreover, monometallic Pt/TiO_2 and Au/TiO_2 were also tested as reference catalysts: it was found that monometallic Pt showed intermediate activity (41 converted mol of glycerol (Pt mol)$^{-1}$ h^{-1}), whereas monometallic Au was inactive (1 converted mol of glycerol (Au mol)$^{-1}$ h^{-1}). These findings indicate that Au has a synergist effect on the activity of Pt, maximized in the case of TiO_2 support.

In addition, the comparison of the reaction profile of the two most active catalysts put in evidence that AuPt/TiO_2 showed a better resistance to deactivation than AuPt/MgO (Figure 1). Interestingly, AAS analysis revealed the presence of Au, Pt and Mg in the reaction media as for AuPt/MgO, whilst AuPt/TiO_2 did not show any leaching. Moreover, the performance of bimetallic AuPt compared to monometallic Pt on TiO_2 (Table 1) showed not only the better activity of the bimetallic sample but also its better resistance to deactivation (Figure 1). Therefore, these results demonstrate that the addition of Au to Pt is beneficial in terms either of activity or of stability in glycerol hydrogenolysis when TiO_2 is used as support, similarly as previously observed for glycerol oxidation [16,17]. Similar findings were achieved by some of us when Au was added to Ru supported on active carbon (AC), with AuRu/AC displaying a higher activity than Ru/AC in glycerol hydrogenolysis to 1,2-PD [15].

As for the obtained selectivity, also reported in Table 1, it was found that AuPt supported on MgO and TiO_2 were extremely selective toward the formation of 1,2-PD (93 and 90%, respectively. All the other catalysts showed a lower selectivity to 1,2-PD (30-50%). In particular, these catalysts produced high amounts of EG and methanol deriving from the C-

C cleavage (see Scheme 1 and Table 1). Moreover, 1-propanol and 2-propanol, deriving from the over-hydrogenolysis of 1,2-PD (Scheme 1, Table 1) were produced in the presence of the AuPt/H-Mordenite and AuPt/S-ZrO_2 catalysts.

A combined HRTEM and FTIR characterization was considered out to unravel on one hand, the influence of both AuPt morphology and size and, on the other hand, to focus on the effect of the nature of the support on the catalytic activity and selectivity. For the latter reason, due to the low stability of MgO based catalyst during the reaction, the attention will be entirely focused on the acid catalysts which all presented a pretty good stability as shown for TiO_2.

A detailed HRTEM characterization of the bimetallic AuPt catalysts has been previously reported in ref. 25 for AuPt/TiO_2 and in ref 16 for all the other catalysts. In all cases, TEM images revealed a good AuPt dispersion and EDS analysis performed showed the exclusive presence of AuPt alloyed nanoparticles [16, 25]. HAADF images of AuPt/TiO_2 catalyst are shown in Figure 2 for the sake of clarity. A representative STEM-HAADF image of AuPt/TiO_2 and the corresponding XEDS elemental analysis are also reported in Figure 3, sections a and section b, respectively. It is clearly shown that both Pt and Au are present in the same nanoparticle. Moreover, the distribution profiles of the metals shown in section c confirmed the coexistence of Pt and Au within the nanoparticle, suggesting the formation of a random gold-platinum alloy structure.

Despite the same alloy nanostructure, however the AuPt bimetallic nanoparticles differ in term of size, as restored in Table 1. Indeed, AuPt/TiO_2 average diameter is 3.7 nm whereas for all the remaining supports larger AuPt nanoparticles with mean diameter of about 6-7.5 nm were observed. The two metals have been deposited on the different support by following the same synthetic procedure summarized in Scheme 3: it is evident that the main difference in the particle size was observed when Pt and Au were supported on TiO_2. Therefore in the case of AuPt/TiO_2, the support played an active role during the metal insertion. Indeed, a

combined scanning tunnelling microscopy and density functional theory study demonstrated that bridging oxygen vacancies are the active nucleation sites for Au clusters on the rutile TiO_2 (110) surface [26]. In particular, by monitoring the temperature dependence of the cluster size distribution and the oxygen vacancy density, it was found that a single Au atom-vacancy complex is stable up to room temperature and a single oxygen vacancy can bind 3 Au atoms on average. For larger clusters, the Au-substrate interface contains a high density of oxygen vacancies, which enhances the binding of Au particles to the substrate. A synthesis model involving the gold nucleation and growth on the oxygen vacancies of titania during the preparation (Scheme 3) can be proposed. These preformed nanoparticles will act themselves as nucleation sites for the Pt precursor, according to the EDS findings showing exclusively the presence of AuPt alloyed nanoparticles on all the catalysts [17, 25].

It is well known that smaller nanoparticles are more active than larger ones in liquid phase reactions, probably due to the higher amount of exposed atoms [1-3]. Keeping this observation in mind, in order to rule out the effect of the particle size and to focus on the support effect, the activity was calculated normalizing by the fraction of exposed atoms (Table 1). In that case, the most active catalyst was AuPt/MgO, in agreement with what reported in the literature, i.e. that metal nanoparticles on basic supports are more active than on acid ones for this reaction [7-9, 27]. The AuPt/MgO catalyst resulted also very selective toward the formation of 1,2-PD (93%) with a small amount of EG and methanol produced (Table 1). Under basic conditions, it was reported that the formation of 1,2-PD proceeded via dehydrogenation of glycerol to glyceraldehyde as firs step (Scheme 2) [7-8]. The limited formation of EG can be due to the difficulty for the retrol-aldol reaction of glyceraldehyde to take place under alkaline conditions [7].

To be noted that the value obtained for AuPt/TiO_2 is very closed to the one of AuPt/MgO (Table 1).

The normalized activity seems to decrease by increasing the support activity. Therefore, to elucidate the effect of the nature of the support on the catalytic performance, a detailed characterization of the surface properties of the catalysts has been performed, in particular by focusing on the acid supports.

The normalised FTIR spectra collected on the different catalysts exposed to 2 mbar 2,6-DMP at r.t. and after 30 min outgassing at the same temperature are shown in the wavenumber range 1500–1700 cm^{-1}, (dotted curves in Figures 4-8). It is worth noting that the use of 2,6-DMP allowed to characterise both Lewis and Brønsted acidic centers present at the surface and offered the advantage to distinguish Lewis and/or Brønsted sites of different acidic strength [28, 29].

The former species, together with H-bonded species, gave rise to three bands in the 1620-1580 cm^{-1} range, where the 8a and 8b ring stretching modes can be observed [30]. The presence of the latter species, i.e. Brønsted sites, was revealed by the formation of the 2,6-dimethylpyridinium species (2,6-$DMPH^{+}$), that presented the 8a-8b bands of the ring stretching modes, at 1640-1655 cm^{-1} and about 1630 cm^{-1}, respectively. A careful deconvolution of the normalised spectra collected upon interaction with 2,6-DMP and after outgassing at r.t. for 30 minutes was carried out (see Figures 4-8) and the calculated integrated areas of the produced absorption bands (normalized to the weight of the pellets and to the SSA) are reported in Table 2. This allowed us to compare the obtained quantitative information about the different acidic sites present on the catalysts and to afford structure-activity correlations with the catalytic results reported in Table 1.

Complex bands related to liquid like and H-bonded 2,6-DMP were produced upon 2,6-DMP adsorption at r.t.. (see Figures 4-8). Therefore, the 2,6-DMP interaction was given mainly via H bonding with the OH groups exposed on the surface of the samples, suggesting that OH groups with weak acid strength play a role in the C-C cleavage to produce EG and methanol (see Tables 1 and 2). This is not true in the case of $AuPt/TiO_2$, which exposed

almost exclusively Lewis sites, according to the residual intensities of the bands after outgassing (given by the integrated areas in Table 2).

No Lewis and Brønsted acidity was observed in the case of AuPt/MCM-41 and AuPt/SiO_2 (the total normalised area of the bands related to H-bonded & physisorbed species was 12.783 and 18.91, respectively). The higher stability to the outgassing shown by the bands related to AuPt/MCM-41, with respect to those detected on AuPt/SiO_2, was due to the presence of mesopores, where the H-bonded 2,6-DMP can be removed only by prolonging the outgassing time (data not shown for the sake of brevity).

On the contrary, both Lewis and Brønsted acid sites were observed on AuPt/S-ZrO_2 (total normalised areas 1.831 and 8.368, respectively) and AuPt/TiO_2 (total normalised areas 4.401 and 8.472, respectively), whereas AuPt/H-Mordenite showed almost exclusively Brønsted acidity (2.38). Interestingly, as revealed by the deconvolution of the spectra collected after outgassing for 30 minutes at r.t., the amount of Lewis sites present on AuPt/TiO_2 was higher than that obtained for AuPt/S-ZrO_2, where the sulphate groups are occupying these sites. Moreover, the apparent absence of Lewis sites on the AuPt/H-Mordenite catalyst was ascribed to the presence of residual water molecules adsorbed on H-Mordenite activated by simply outgassing at 120 °C for 1 hour.

Table 2. Position and integrated areas of the bands observed upon 2,6-DMP dosage at r.t..

	Band integrated areas of adsorbed 2,6-DMP					
	Brønsted acid sites			H-bonded	physisorbed	H-bonded & physisorbed
Position (cm^{-1})	1648	1640	1632	1603	1595	1581
AuPt/MCM-41				2.404	5.256	5.123
AuPt/SiO_2				5.169	2.022	11.719
	Brønsted acid sites			Lewis acid sites & H-bonded	physisorbed	H-bonded & physisorbed
AuPt/S-ZrO_2[a]	3.480	3.186	1.702	2.384	2.318	6.609
	6.444		5.832	1.046		0.785

$AuPt/TiO_2$[a]	3.621	3.808	1.043	5.318	7.073	14.738
	0.377	2.111	0.429	2.443	0.632	1.326
AuPt/H-Mordenite[a]	0.365	0.107	1.908	0.9286	0.200	1.616
	1.334		1.688			

[a] The deconvolution was performed also on the spectra collected after 30 minutes outgassing at r.t. (refer to the second line for each catalyst).

On the basis of the IR results, it has been related the low selectivity to 1,2-PD displayed by both AuPt/S-ZrO_2 and AuPt/H-Mordenite to the presence of Brønsted sites, that are able to give over-hydrogenolysis of 1,2-PD, forming 1-propanol and 2-propanol. Very recently, a high 1,3-PD selectivity (48.6 %) in the presence of a 2 wt % Pt/H-mordenite catalyst at 94.9 % glycerol conversion was also reported [18]. The selectivity to 1,3-PD was influenced by the Pt dispersion (around 4 nm) and by the Brønsted acidity of the support. In our case, for the AuPt/H-Mordenite catalyst, an effect on the selectivity to 1,2-PD due to the additional presence of gold, that acts on the electronic properties of Pt, can be inferred.

Interestingly, Brønsted sites are also present at the surface of $AuPt/TiO_2$, i.e. the most active catalyst (according to Table 1). Our results gave precise indication that despite the amount of these sites is comparable to that detected on AuPt/S-ZrO_2 and higher than that observed for AuPt/H-Mordenite, the behaviour towards the outgassing at r.t. is completely different. Indeed, on both AuPt/S-ZrO_2 (Figure 6) and AuPt/H-Mordenite (Figure 7) the amount of Brønsted sites is enhanced after outgassing (the integrated area values move from 8.368 up to 12.276 and from 2.38 up to 3.022, respectively) indicating that at low coverages a rearrangement of the 2,6-DMP molecules on the most acidic sites has occurred. On the contrary, a decrease in intensity of the bands related to the Brønsted sites is observed in the case of $AuPt/TiO_2$ (from 8.472 down to 2.917, see Figure 8), giving evidence of the presence of less strong Brønsted sites on this catalyst.

On the contrary, the FTIR spectroscopic characterisation indicated that the superior activity as well as the high selectivity displayed by $AuPt/TiO_2$ can be related to the presence of

Lewis sites with moderate strength. More acidic supports present a lower activity. Similar results were reported in the literature by Zhang et al. [31]. Indeed, they reported that Cu immobilized on alumina with moderate acid sites is more active than more acidic zeolite supports.

Conclusion

Bimetallic AuPt catalysts were tested in the glycerol hydrogenolysis, using supports with different acid-base properties. It was found that the smallest AuPt nanoparticles (with average diameter equal to 3.7 nm) showed a better activity than largest ones (6-7 nm). However, normalizing the activity (conversion) for the number of exposed atoms, it appears clearly that the activity and the selectivity were significantly influenced by the acid base properties of the support. AuPt on MgO, as expected, appears the most active even it deactivates quite rapidly. The order of activity in the case of acidic support ($AuPt/TiO_2$) > ($AuPt/MCM41 \geq AuPt/SiO_2$) > ($AuPt/H\text{-}Mordenite > AuPt/S\text{-}ZrO_2$) can be directly related to the acid character of the support: the higher the strength of the acidic sites, the lower the activity. In particular, the presence of Lewis sites is required for achieving good catalytic performances. Moreover, it was shown that the nature of the acidic sites plays also an important role in tailoring the selectivity, by lowering the production of 1,2-PD and by directing the glycerol hydrogenolysis reaction to EG and methanol by C-C cleavage and/or 1-propanol and 2-propanol by over-hydrogenolysis of 1,2-PD. Moreover it has been shown that the intermediate acidic character of TiO_2 leads to an improved

References

1. P. Gallezot, (2012) Chem. Soc. Rev. 41: 1538-1558.
2. G. W. Huber, S. Iborra and A. Corma, (2006) Chem. Rev., 106: 4044-4098.

3. A. Corma, S. Iborra and A. Velty, (2007) Chem. Rev. 107: 2411-2502.
4. B. Katryniok, H. Kimura, E. Skrzyńska, J.-S. Girardon, P. Fongarland, M. Capron, R. Ducoulombier, N. Mimura, S. Paul, F. Dumeignil, (2011) Green Chem. 13: 1960-1979.
5. S. E. Davis, M. S. Ide, R. J. Davis, (2013) Green Chem. 15: 17-45.
6. A. Villa, N. Dimitratos, C. E. Chan-Thaw, C. Hammond, L. Prati, G. J. Hutchings, (2015) Acc. Chem. Res. 48 (5): 1403-1412.
7. Y. Nakagawa, K. Tomishige, (2011) Catal. Sci. Technol. 1: 179-190.
8. Y. Nakagawa, M. Tamura and K. Tomishige, (2014) J. Mater. Chem. A 2: 6688-6702.
9. Y. Wang, J. Zhou, X. Guo, (2015) RSC Adv. 5: 74611-74628.
10. A. Martin, U. Armbruster, I. Gandarias and P. L. Arias, (2013) Eur. J. Lipid Sci. Technol. 115: 9-27.
11. C.-H. Zhou, J. N. Beltramini, Y.-X. Fan and G. Q. Lu, (2008) Chem. Soc. Rev. 37: 527-549.
12. H. Yue, Y. Zhao, X. Ma, J. Gong, (2012) Chem. Soc. Rev. 41: 4218-4244.
13. M. A. Dasari, P.-P. Kiatsimkul, W. R. Sutterlin and G. J. Suppes, (2005) Appl. Catal. A, 281: 223-231.
14. M. L. Barbelli, G. F. Santori and N. N. Nichio, (2012) Bioresour. Technol. 111: 500-503.
15. A. Villa, G.M. Veith and L. Prati, (2010) Angew. Chem. Int. Ed. 49: 4499-4502.
16. A. Villa, S. Campisi, K. M. H. Mohammed, N. Dimitratos, F. Vindigni, M. Manzoli, W. Jones, M. Bowker, G. J. Hutchings, L. Prati, (2015) Catal. Sci. Technol. 5: 1126-1132.
17. S. Shanthi Priya, P. Bjanuchander, V. Pavan Kumar, D.K. Dumbre, S.R. Periasamy, S.K. Bhargava, M. Lakshmi Kantam, (2016) ACS Sustainable Chem. Eng. 4: 1212-1222.
18. T. Miyazawa, Y. Kusunoki, K. Kunimori and K. Tomishige (2006) J. Catal. 240: 213-221.
19. C. Montassier, J. C. Menezo, J. Moukol and J. Naja (1991) J. Mol. Catal. 70: 65-84.
20. Y. Nakagawa, Y. Shinmi, S. Koso and K. Tomishige (2010) J. Catal., 272: 191-194.
21. K. M. S. Khalil, (2007) J. Colloid Interf. Sci. 315: 562-569.
22. K. Mori, T. Hara, T. Mizugaki, K. Ebitani, K. Kaneda (2004) J. Am. Chem. Soc. 126: 10657-10666.

23. N. Dimitratos, A. Villa, L. Prati, C. Hammond, C. E. Chan-Thaw, J. Cookson, P. T. Bishop, (2016) Appl. Catal. A 514: 267-275.
24. A. Villa, C. E. Chan-Thaw, S. Campisi, C. L. Bianchi, D. Wang, P. G. Kotula, C. Kuebel, L. Prati (2015) Phys. Chem. Chem. Phys. 17: 28171-28176.
25. C. E. Chan-Thaw, L. E. Chinchilla, S. Campisi, G. A. Botton, L. Prati, N. Dimitratos, A. Villa (2015) ChemSusChem, 8: 4189-4194.
26. E. Wahlström, N. Lopez, R. Schaub, P. Thostrup, A. Rønnau, C. Africh, E. Lægsgaard, J. K. Nørskov, F. Besenbacher (2004) Phys. Rev. Lett. 303, 026101-1 - 026101-4.
27. J. ten Dam, U. Hanefeld (2011) ChemSusChem 4: 1017-1034.
28. C. Morterra, G. Meligrana, G. Cerrato, V. Solinas, E. Rombi, M.F. Sini, (2003) Langmuir, 19: 5344-5356.
29. J.A. Toledo-Antonio, M.A. Cortés-Jácome, J. Navarrete, C. Angeles-Chavez, E. López-Salinas, A. Rendon-Rivera, (2010) Catal Today 155: 247-254.
30. C. Morterra, G. Cerrato, G. Meligrana, (2001) Langmuir, 17: 7053-7060.
31. L. Y. Guo, J. X. Zhuo, J. B. MaO, X. W. Guo, S. G. Zhang, (2009) Appl. Catal. A: Gen. 367: 93-98.

Figure 1 Reaction profile of AuPt catalysts

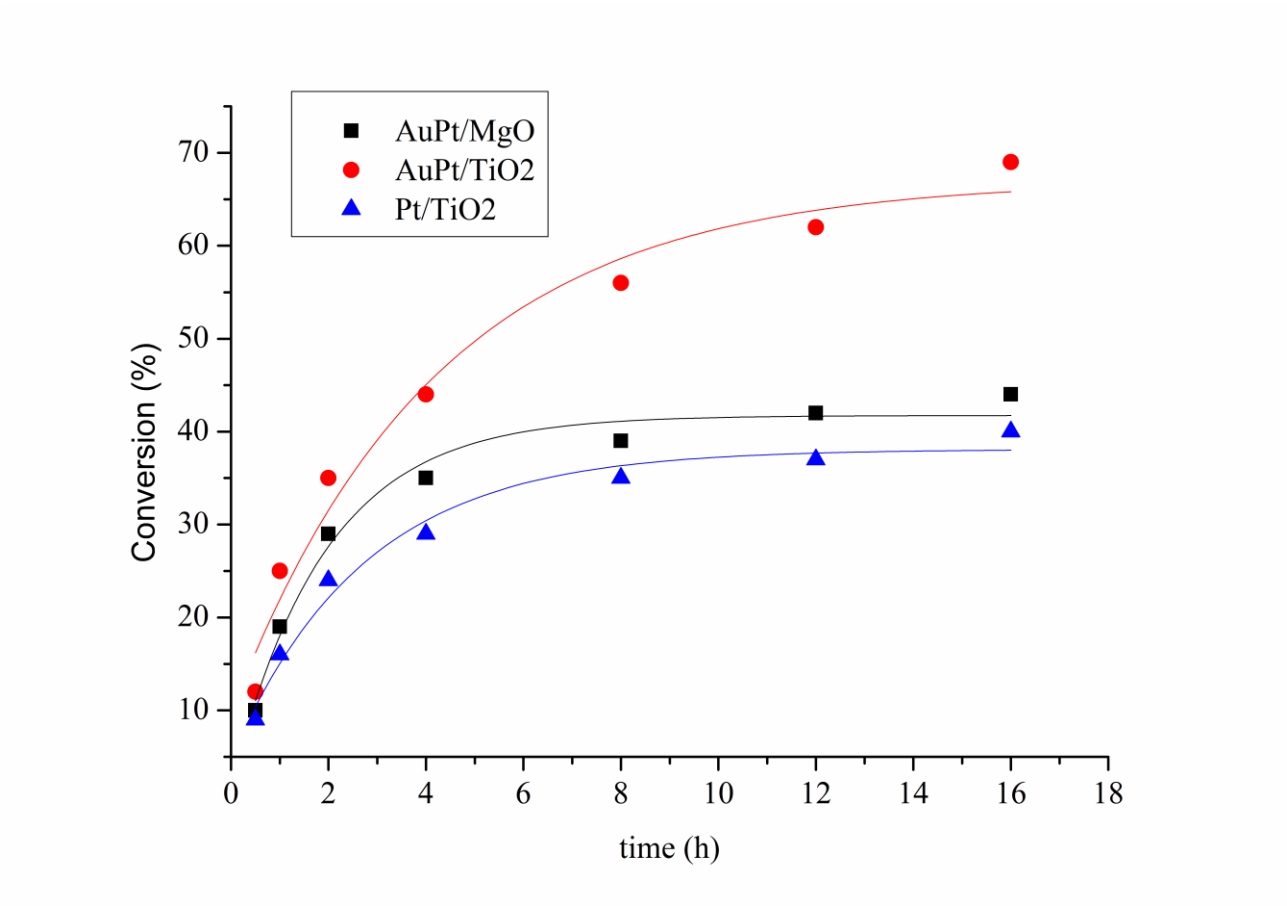

Figure 2. HAADF images of $AuPt/TiO_2$. Images, (a) and (b), show the presence of nanoparticles ca. 3.7 nm in size.

a) 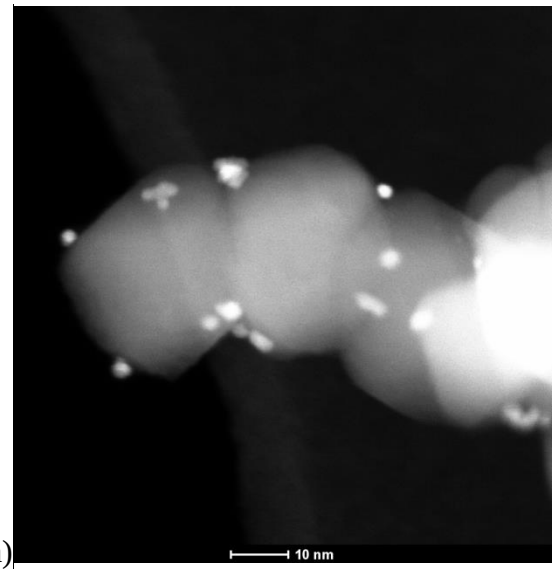

b) 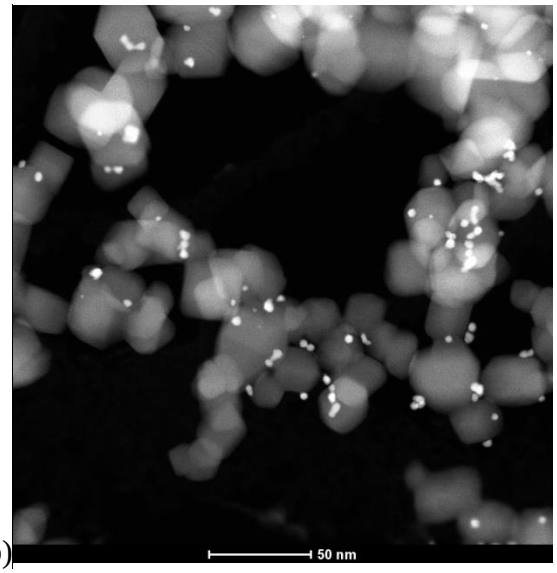

Figure 3 (a) STEM-HAADF image (b) and the corresponding XEDS spectra taken from the AuPt nanoparticle. (c) The corresponding Au Lα and Pt Lα linescan profile taken across the diameter of the same AuPt nanoparticle (dashed orange harrow in section a).

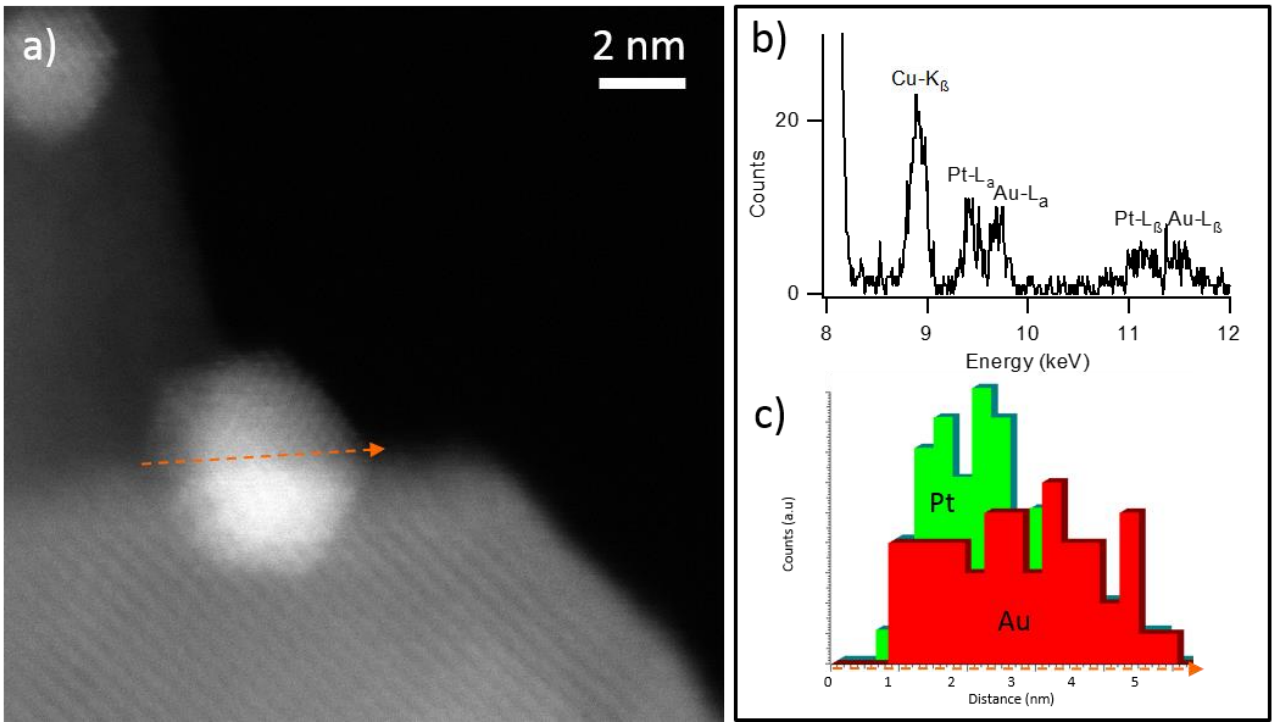

Figure 4. FTIR difference spectrum reported in the spectral region of 8a-8b ring modes of 2,6-DMP collected exposed to 2,6- DMP (2 mbar) at r.t. on AuPt/MCM-41 (blue dotted curve), curvefit of the spectrum (orange curve) and deconvoluted bands (grey curves).

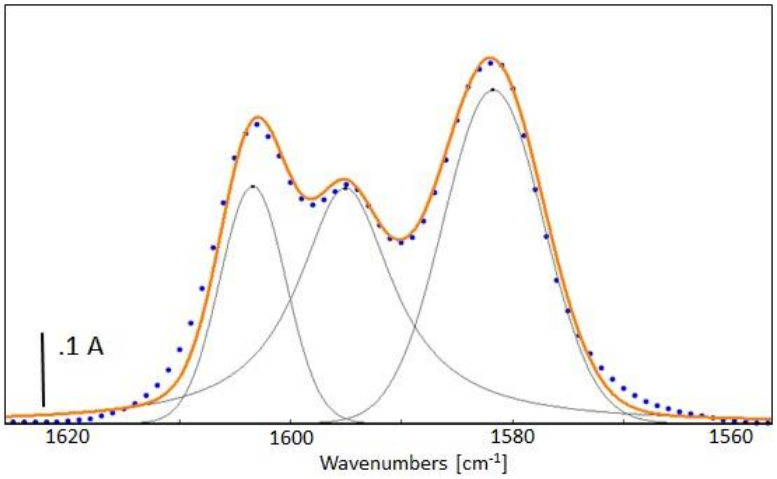

Figure 5. FTIR difference spectrum reported in the spectral region of 8a-8b ring modes of 2,6-DMP collected after the inlet of 2,6- DMP (2 mbar) at r.t. on AuPt/SiO_2 (blue dotted curve), curvefit of the spectrum (orange curve) and deconvoluted bands (grey curves).

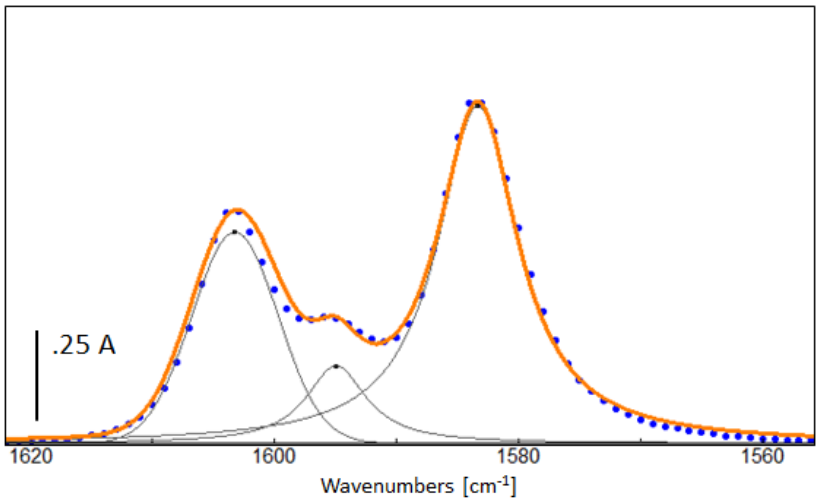

Figure 6. FTIR difference spectrum reported in the spectral region of 8a-8b ring modes of 2,6-DMP collected after the inlet of 2,6- DMP (2 mbar) at r.t. and (inset): after 30 minutes outgassing, on AuPt/S-ZrO_2 (blue dotted curves), curvefits of the spectra (orange curves) and deconvoluted bands (grey curves).

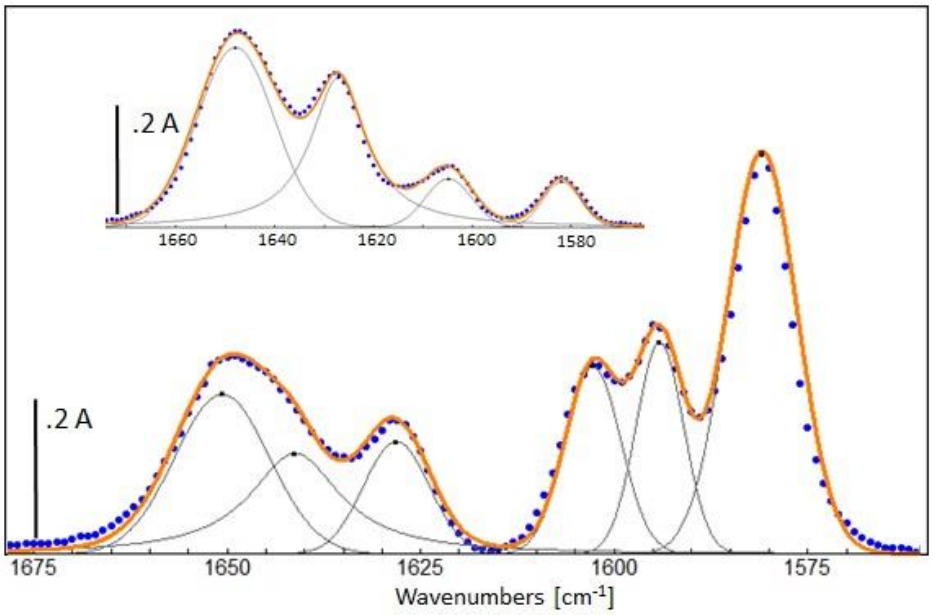

Figure 7. FTIR difference spectrum reported in the spectral region of 8a-8b ring modes of 2,6-DMP collected after the inlet of 2,6- DMP (2 mbar) at r.t. and (inset): after 30 minutes outgassing, on AuPt/H-Mordenite (blue dotted curves), curvefits of the spectra (orange curves) and deconvoluted bands (grey curves).

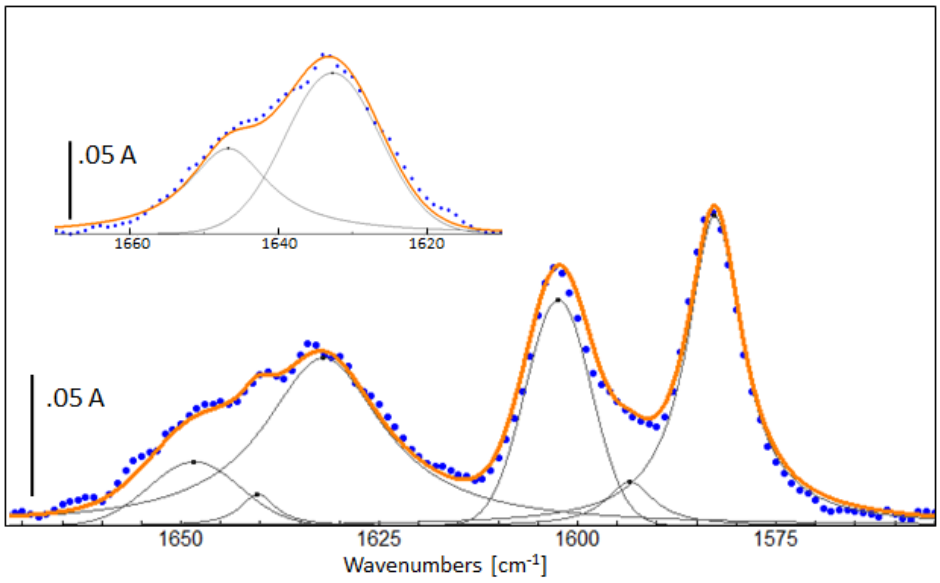

Figure 8. FTIR difference spectrum reported in the spectral region of 8a-8b ring modes of 2,6-DMP collected after the inlet of 2,6- DMP (2 mbar) at r.t. and (inset): after 30 minutes outgassing, on $AuPt/TiO_2$ (blue dotted curves) , curvefits of the spectra (orange curves) and deconvoluted bands (grey curves).